

Intravasation-On- μ Device (INVADE): Engineering Dynamic Vascular Interfaces to Study Cancer Cell Intravasation

Fengtao Jiang, Yingqi Zhang, Guocheng Fang, Yao Wang, Alexander Dupuy, Jasmine Jin, Yi Shen, Khoon S Lim, Yinyan Wang, Yu Shrike Zhang, Ann-Na Cho, Hongxu Lu,* and Lining Arnold Ju*

Cancer metastasis begins with intravasation, where cancer cells enter blood vessels through complex interactions with the endothelial barrier. Understanding this process remains challenging due to the lack of physiologically relevant models. Here, INVADE (Intravasation-on- μ Device), a biomimetic microfluidic platform, is presented, enabling high-throughput analysis of cancer cell intravasation under controlled conditions.

This engineered platform integrates 23 parallel niche chambers with an endothelialized channel, providing both precise microenvironmental control and optical accessibility for real-time visualization. Using this platform, distinct intravasation mechanisms are uncovered: MCF-7 cells exhibit collective invasion, while MDA-MB-231 cells demonstrate an interactive mode with three functionally distinct subpopulations. A previously unknown epithelial-mesenchymal transition (EMT) and mesenchymal-epithelial transition (MET) switch is discovered during intravasation, where MDA-MB-231 cells initially increase Vimentin expression before undergoing a 2.3 fold decrease over 96 h alongside a 1.5 fold increase in epithelial cell adhesion molecule (EpcAM). Remarkably, endothelial cells directly suppress cancer cell mesenchymal properties, as evidenced by a 4.6 fold reduction in Vimentin expression compared to mono-cultures. Additionally, bilateral cancer-endothelial interactions are revealed, aggressive cancer cells induce significant intercellular adhesion molecule-1 (ICAM-1) upregulation in endothelium. The INVADE platform represents an engineering advancement for studying complex cell–cell interactions with implications for understanding metastatic mechanisms.

1. Introduction

Cancer metastasis remains the leading cause of cancer-related mortality, accounting for $\approx 90\%$ of deaths among cancer patients.^[1] Metastasis involves the dissemination of cancer cells from the primary tumor to distant organs via intravasation—where cancer cells transigrate across the endothelial barrier to enter the bloodstream—serving as a critical early step in this process.^[2,3]

The complexity of cancer cell intravasation stems from intricate bilateral interactions between cancer cells and the endothelium.^[3–5] Traditional studies have identified key molecular players, including adhesion molecules (e.g. selectins and integrins) and signaling pathways that mediate cancer-endothelial interactions.^[6–8] However, emerging evidence highlights the critical role of microenvironment in regulating intravasation efficiency.^[9,10] The vascular microenvironment presents unique mechanical challenges, including fluid shear stress (0.5–10 dyne cm^{-2}), varying vessel geometries, extracellular matrix stiffness, and endothelial barrier mechanics, all of which significantly influence cancer cell behavior.^[11–13]

F. Jiang, Y. Zhang, Y. Wang, A. Dupuy, J. Jin, Y. Wang, A.-N. Cho, L. A. Ju
School of Biomedical Engineering
Faculty of Engineering
The University of Sydney
Darlington, NSW 2008, Australia
E-mail: arnold.ju@sydney.edu.au

G. Fang
School of Electrical & Electronic Engineering Nanyang Technological
University
50 Nanyang Avenue, Singapore 639798, Singapore

Y. Wang, A. Dupuy, K. S Lim, L. A. Ju
Charles Perkins Centre
The University of Sydney
Camperdown, NSW 2006, Australia

Y. Wang, A.-N. Cho, L. A. Ju
The University of Sydney Nano Institute (Sydney Nano)
The University of Sydney
Camperdown, NSW 2006, Australia

Y. Shen
School of Chemical and Biomolecular Engineering
Faculty of Engineering
The University of Sydney
Darlington, NSW 2008, Australia

 The ORCID identification number(s) for the author(s) of this article can be found under <https://doi.org/10.1002/adma.202501466>

© 2025 The Author(s). Advanced Materials published by Wiley-VCH GmbH. This is an open access article under the terms of the [Creative Commons Attribution](https://creativecommons.org/licenses/by/4.0/) License, which permits use, distribution and reproduction in any medium, provided the original work is properly cited.

DOI: 10.1002/adma.202501466

Moreover, different cancer types exhibit distinct metastatic potentials, indicating that cell type-specific mechanisms govern intravasation.^[3,14,15] For instance, breast cancer cells such as MDA-MB-231 and MCF-7 demonstrate markedly different invasive behaviors *in vivo*.^[16] Each cancer type, with unique biological properties and migratory patterns, directly impacts the metastatic potential, clinical outcomes, and treatment responses. Recognizing these differences enables more precise interventions, personalized treatment approaches, and better prognostic assessments.

More importantly, the epithelial-mesenchymal transition (EMT), a key process in metastasis that drives cell migration, invasion, and the formation of secondary tumors, remains incompletely understood due to its multifaceted and dynamic nature. EMT involves a series of tightly regulated and reversible steps that are influenced by genetic, molecular, and environmental factors. Despite extensive research, significant gaps persist in understanding how tissue context, cellular heterogeneity, and mechanical cues in the microenvironment contribute to the initiation, progression, and differentiation of cancer cell subpopulations.^[4,17–19]

Current approaches for studying cancer intravasation face critical limitations. While *in vivo* models are physiologically relevant, they often lack the temporal and spatial resolution required to observe detailed cellular interactions.^[4,20] Traditional *in-vitro* systems, such as Transwell assays, fail to recreate the complex microenvironment of blood vessels and cannot fully capture dynamic cell–cell interactions.^[21,22] Furthermore, these systems typically focus on endpoint analyses, missing crucial information about the temporal progression of cancer-endothelial interactions.^[23]

Recent advancements in microfluidic technology have led to the development of platforms that provide precise control over mechanical and chemical parameters, closely mimicking physi-

ological conditions.^[13,24,25] However, many existing platforms focus primarily on the later stage of the metastasis cascade, neglecting intravasation as an early and critical event. Additionally, many of these platforms either lack the capability for high-throughput analysis or fail to incorporate key features of the vascular microenvironment, such as controlled flow conditions and intact endothelial barrier establishment.^[26,27] The potential existence of bilateral communication between cancer cells and endothelial cells has not been sufficiently investigated either.^[28,29]

To address these challenges, there is a pressing need for *in-vitro* models that accurately recreate the vascular microenvironment while allowing high-resolution, real-time monitoring of the intravasation process.^[30,31] Such platforms should integrate precise control over the tumor micro-environment with the capability to monitor dynamic cell–cell interactions in real-time while maintaining sufficient throughput for robust statistical analysis. Here, we present the INVADE (Intravasation-on- μ Device) platform—an innovative 3D microfluidic system designed specifically to investigate the real-time cancer-endothelial interactions during the intravasation process under physiologically relevant conditions.

2. Results

2.1. INVADE Platform Design and Implementation for High-Throughput Cancer Intravasation Analysis

To mimic the process of intravasation, we engineered a sophisticated microfluidic device that integrates multiple cancer cell niches with an endothelialized channel, enabling high-throughput observation of cancer-endothelial interactions (Figure 1A–C; Figures S1 and S2, Supporting Information). Specifically, this novel microfluidic platform features an array of 23 identical niche chambers (radius: 75 μm) connected to the main channel through constriction necks (width: 40 μm , length: 255 μm , cross-sectional area: 12 000 μm^2) that impose contraction-like confinement, mimicking the physical barriers encountered by cancer cells *in vivo* (Figure 1C). The main channels (width: 300 μm , height: 200 μm) were designed to recapitulate vasculature and maintain physiological flow conditions (shear stress: 0.5–10 dyne cm^{-2} , Figure 1D; Figure S3, Supporting Information). This architecture provides physiologically relevant mechanical constraints during cancer cell intravasation while maintaining experimental consistency across multiple chambers, allowing for robust and reproducible studies of cancer cell dynamics under controlled conditions. The INVADE represents an innovative platform for studying cancer cell entry into blood vessels by replicating the *in-vivo* environments encountered during intravasation.

To validate the INVADE platform's functionality, we performed co-culture experiments using fluorescently labeled MDA-MB-231 breast cancer cells (red) and human umbilical vein endothelial cells (HUVECs, green). Confocal imaging demonstrated the successful establishment of the cancer niche and endothelium compartments, along with their interfaces across multiple chambers simultaneously, confirming the platform's high-throughput capability (Figure 1E). This configuration significantly increases experimental efficiency while maintaining consistent conditions across all observation units.

K. S. Lim
School of Medical Sciences
The University of Sydney
Darlington, NSW 2008, Australia

Y. Wang
Department of Neurosurgery
Beijing Tiantan Hospital
Capital Medical University
Beijing 100070, China

Y. Wang
The George Institute for Global Health
Barangaroo 2000, Australia

Y. S. Zhang
Division of Engineering in Medicine
Department of Medicine
Brigham and Women's Hospital
Harvard Medical School
Cambridge, MA 02139, USA

H. Lu
State Key Laboratory of High Performance Ceramics and Superfine Microstructure
Shanghai Institute of Ceramics
Chinese Academy of Sciences
1295 Dingxi Road, Shanghai 200050, P. R. China
E-mail: hongxu.lyu@mail.sic.ac.cn

L. A. Ju
Heart Research Institute
Camperdown, Newtown, NSW 2042, Australia

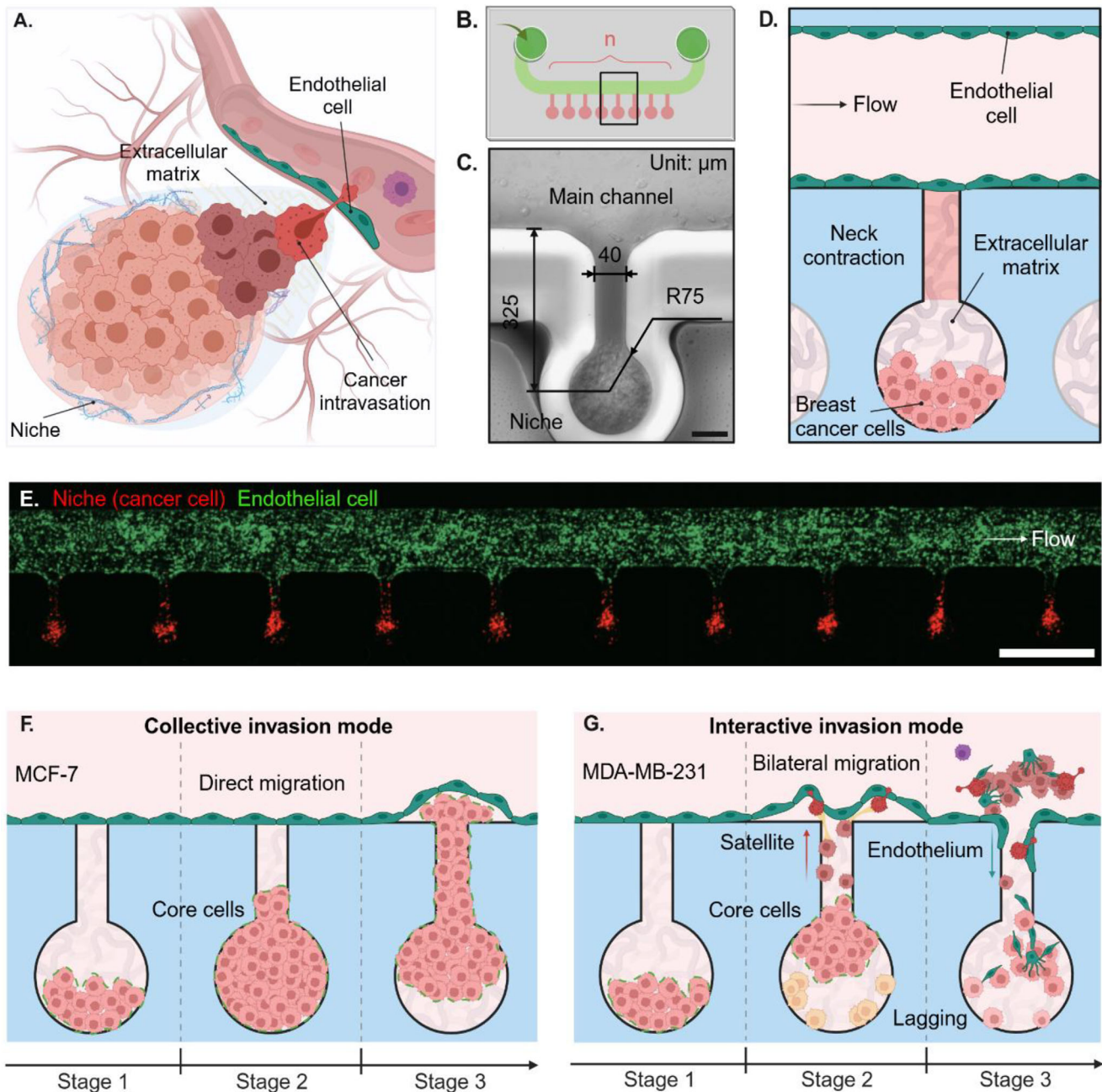


Figure 1. INVADE biomimetic microfluidic platform enabling high-throughput analysis of cancer-endothelial intravasation dynamics. A) Schematic of intravasation as the initial step in the metastasis cascade. B) Graphical illustration of a lab-on-chip device – INVADE to model intravasation of cancer cells to the vasculature. The INVADE platform integrates identical niche chambers ($n = 23$) with an endothelialized channel for high-throughput analysis of cancer-endothelial interactions. C) Zoom-in image of an individual niche chamber connected to the endothelialized channel. Scale bar: 70 μm . D) Schematic of an individual intravasation unit showing main channels (endothelium residence and medium flow), niche chambers (cancer residence), and connecting necks (intravasation paths). E) Confocal image of the INVADE model co-cultured with MDA-MB-231 breast cancer cells (red) and human umbilical endothelial cells (HUVEC, green) demonstrating efficient examination of cancer cell intravasation in a high-throughput setup; scale bar: 500 μm . Conceptual illustration highlighting two distinct intravasation modes: F) collective invasion mode (MCF-7) versus G) interactive invasion mode (MDA-MB-231). Light red cell: core cell; yellow cell: lagging cell; red cell: satellite cell; deep red cell: invading cancer cell; purple cell: escaped cancer cell green cell: endothelial cell. Illustration figures are created at <https://BioRender.com>.

A. Stepwise biofunctionalization of INVADE platform

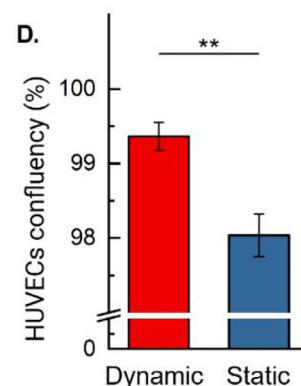
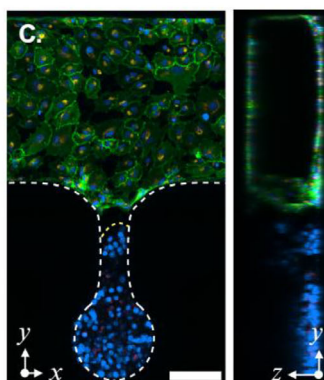
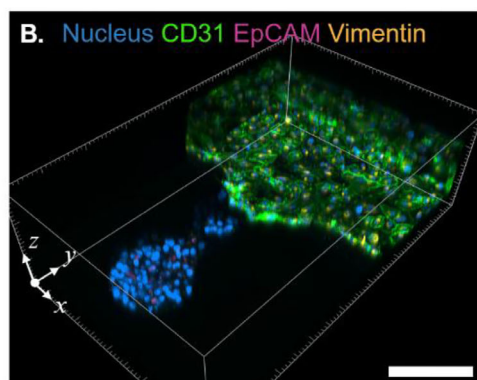
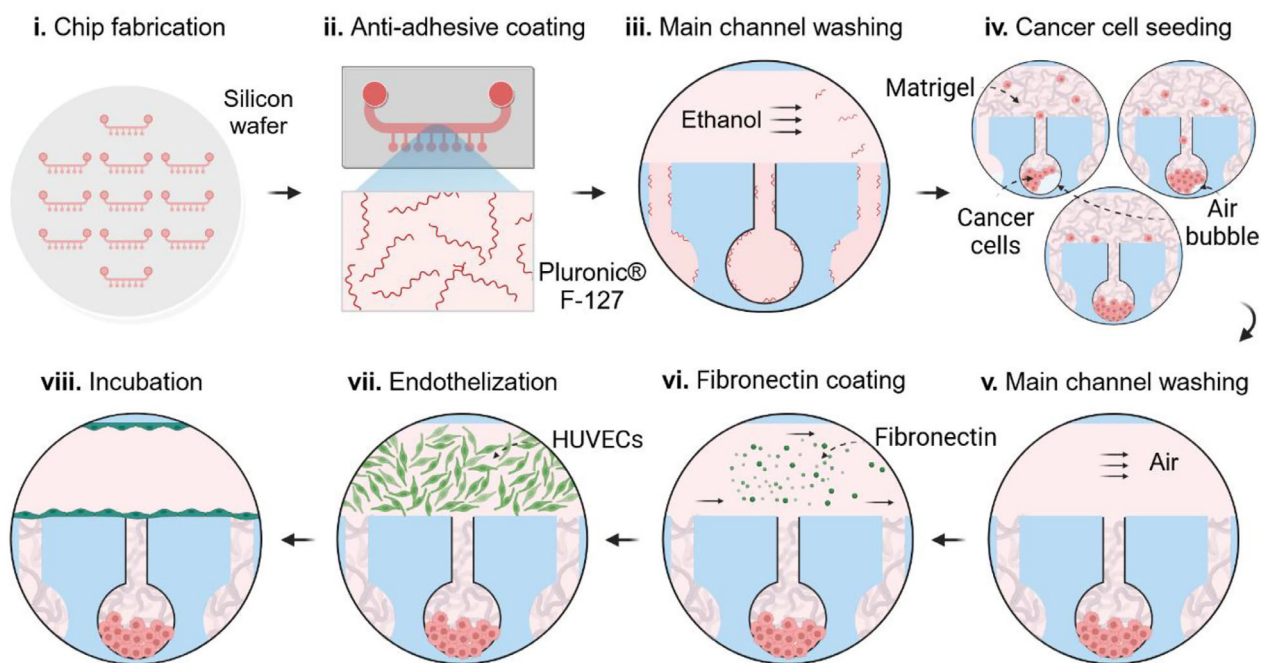


Figure 2. Biofunctionalization strategy establishes INVADE biomimetic microfluidic platform with a functional endothelial barrier. A) Stepwise demonstration of INVADE platform preparation for cancer-endothelial interaction studies. i) Fabrication of INVADE microfluidic platform via soft lithography. ii, iii) Pluronic F-127 treatment for non-adhesive niche chamber to inhibit cancer cell adhesion and promote spheroid formation. iv) Cancer cell and Matrigel mixture seeding into the niche chamber. v) Removal of residual cancer cells and Matrigel mixture from the main channel. vi) Fibronectin coating of the main channel to support endothelial cell attachment. vii) Endothelialization of the main channel with human umbilical endothelial cells (HUVECs). viii) Formation of cancer cell niche and confluent endothelium within the INVADE platform. Confocal images of the B) three-dimensional view, C) top view (left), and side view (right) of the INVADE platform cultured on Day 2. Scale bars: 200 μm (B), 100 μm (C). D) Comparison of HUVEC confluency under dynamic versus static culture conditions. Data are mean \pm SEM. Statistical significance assessed by One-Way ANOVA (** $p < 0.01$; $n \geq 3$). Illustration figures are created at <https://BioRender.com>.

Using the INVADE platform, we revealed two distinct modes of intravasation between different breast cancer cell lines (Figure 1F,G). MCF-7 cells exhibited a collective invasion mode, characterized by cohesive group migration (Figure 1F), while MDA-MB-231 cells demonstrated an interactive invasion mode featuring three distinct cell populations: core cells, satellite cells, and lagging cells (Figure 1G). Each subpopulation plays specific roles in the intravasation process, contributing to the complex dynamics of cancer cell entry into vessels.

2.2. Establishment of Stable Vessel-Mimicking Microenvironment and Validation of Endothelial Barrier Functionality

The development of a stable vessel-mimicking microenvironment in the INVADE platform required a meticulously optimized multi-step fabrication and functionalization protocol (Figure 2A). Initial device fabrication employed standard soft lithography techniques to create precise microchannel arrays essential for vascular architecture mimicry. A critical innovation in our

protocol was the selective surface modification approach, where Pluronic F-127 coating was specifically applied to the niche chamber while maintaining the main channel's capacity for endothelial cell adhesion (Figure 2A,ii,iii).

Prior to cell seeding, devices underwent vacuum treatment (>30 min) to eliminate air bubbles and ensure uniform surface modification. Cancer cells were perfused into the microchannel in the form of a specialized mixture of cell suspension and Matrigel (2:1 volume ratio), carefully optimized to recreate the complex extracellular environment containing laminin, collagen IV, and entactin/nidogen (Figure 2A,iv). Following a 15 min incubation on ice for bubble absorption, cells were centrifuged (2000 rpm, 30 s) to achieve uniform distribution at the chamber bottom. Afterwards, the device was placed in the incubator at 37 °C for 30 min for Matrigel gelation, which allowed the fixation of cancers at the niche chamber.

A crucial innovation in our protocol was the implementation of a repeated Matrigel seeding step after Matrigel gelation, specifically designed to fill the neck constriction and provide support for endothelial attachment to establish a clear endothelial barrier. Residual cells or Matrigel in the main channel were then carefully removed using airflow to maintain the integrity of the separate compartments after 30 mins of incubation at 37 °C (Figure 2A,v). Then 100 µg mL⁻¹ fibronectin was introduced to allow selective coating of the main channel to promote endothelial cell attachment (Figure 2A,vi). Lastly, HUVECs suspension at 1 × 10⁶ cells mL⁻¹ was perfused into the main channel (Figure 2A, vii) and allowed to attach on the channel surface for 30 min (Figure 2A, viii).

The endothelialization process resulted in the formation of a stable, confluent monolayer (Figure 2B,C), achieving over 99% coverage under dynamic culture conditions (Figure 2D). Three-dimensional confocal microscopy confirmed the successful establishment of distinct compartments and clear visualization of the cancer-endothelial interface (Figure 2B). Comparative analysis between dynamic and static culture conditions revealed significantly enhanced endothelial coverage under flow conditions ($p < 0.001$), highlighting the importance of mechanical stimulation for maintaining endothelial integrity (Figure 2C; Figures S4 and S5, Supporting Information).

To validate the integrity and functionality of the endothelial barrier, we performed confocal imaging at different z-positions (50, 100, 150, and 200 µm) along the neck region (Figure S5, Supporting Information). These images confirmed the formation of a continuous endothelial monolayer at the neck-main channel interface, with intact cell-cell junctions, as evidenced by the presence of CD31 staining. Additionally, we conducted diffusion experiments using 3- to 5-kDa FITC-Dex to assess barrier permeability (Figure S6, Supporting Information). In the absence of an endothelial layer, FITC-Dex rapidly diffused into the niche chambers within 30 s. Conversely, the presence of a confluent endothelial layer significantly restricted diffusion even after 60 s, demonstrating effective barrier function. Notably, stimulation with PMA (50 ng mL⁻¹) did not result in a substantial change in diffusion, suggesting the minimal impact of PMA on endothelial permeability.

2.3. Cancer Type-Specific Migration Patterns During Intravasation

Time-resolved imaging using dual fluorescent labeling (PKH67 for HUVECs, PKH26 for cancer cells) revealed fundamentally different invasion modes between two breast cancer cell lines, MCF-7 and MDA-MB-231 cells (Figure 3A,B). MCF-7 cells exhibited collective invasion behavior, maintaining cell-cell contacts throughout the migration process (Figure 3C). In contrast, MDA-MB-231 cells demonstrated an interactive invasion mode characterized by distinct cell populations (Figure 3D). Detailed analysis revealed three MDA-MB-231 subpopulations with unique behaviors (Figure 3D): satellite cells, named for their behavior similar to satellites as they guide subsequent cells throughout intravasation by acting as pioneers to clear the pathway and making initial contact with the endothelial barrier; core cells, which show coordinated margination; and lagging cells, named for their position deep within the niche.^[32] Cancer cell contour profiling quantified these distinct migratory patterns (Figure 3E).

Single-cell morphology analysis of MDA-MB-231 cells during 3–6 h of invasion showed distinct morphological transitions during a relatively short response time (<6 h) (Figure 3F). From 3–4 h, the pink dotted line labeled cell adopted an elongated, spindle-like morphology, characteristic of the mesenchymal phenotype, enabling it to penetrate dense ECM regions. This elongation facilitates movement through narrow spaces within the matrix. At 5-h time mark, the cell transformed into an “octopus-like” structure, extending multiple protrusions or filopodia. These extensions increase the cell's surface area, enhancing its ability to sense and respond to environmental cues, such as chemotactic signals or variations in ECM stiffness. At 6 h time mark, the cell exhibited a “snail-like” morphology, characterized by a polarized shape with a broad leading edge and a contracted rear. This configuration is optimized for amoeboid movement, allowing rapid translocation and efficient navigation through the ECM.^[33] These morphological adaptations are indicative of cell plasticity and their ability to switch between different modes of migration in response to microenvironmental cues.

Further, velocity profiling demonstrated significant differences between subpopulations (Figure 3G,H), with satellite cells showing the highest motility (24.1 µm h⁻¹) compared to core cells (6.7 µm h⁻¹) and lagging cells (17.6 µm h⁻¹). The observed morphological transformations and sub-population-dependent velocity profile suggest that MDA-MB-231 cells possess a high degree of phenotypic plasticity, enabling them to adapt their migration strategies during intravasation. This adaptability is a hallmark of aggressive cancer cells and is associated with increased metastatic potential. By modulating their shape and migratory mechanisms, these cells can effectively traverse the ECM, breach endothelial barriers, and enter the circulatory system, thereby facilitating the dissemination to distant sites.^[34] The INVADE platform provides the observation window for the complex interplay of intracellular signaling pathways and interactions within the ECM, including cytoskeletal remodeling,^[35,36] extracellular matrix interactions,^[37,38] signaling pathways,^[39] etc.

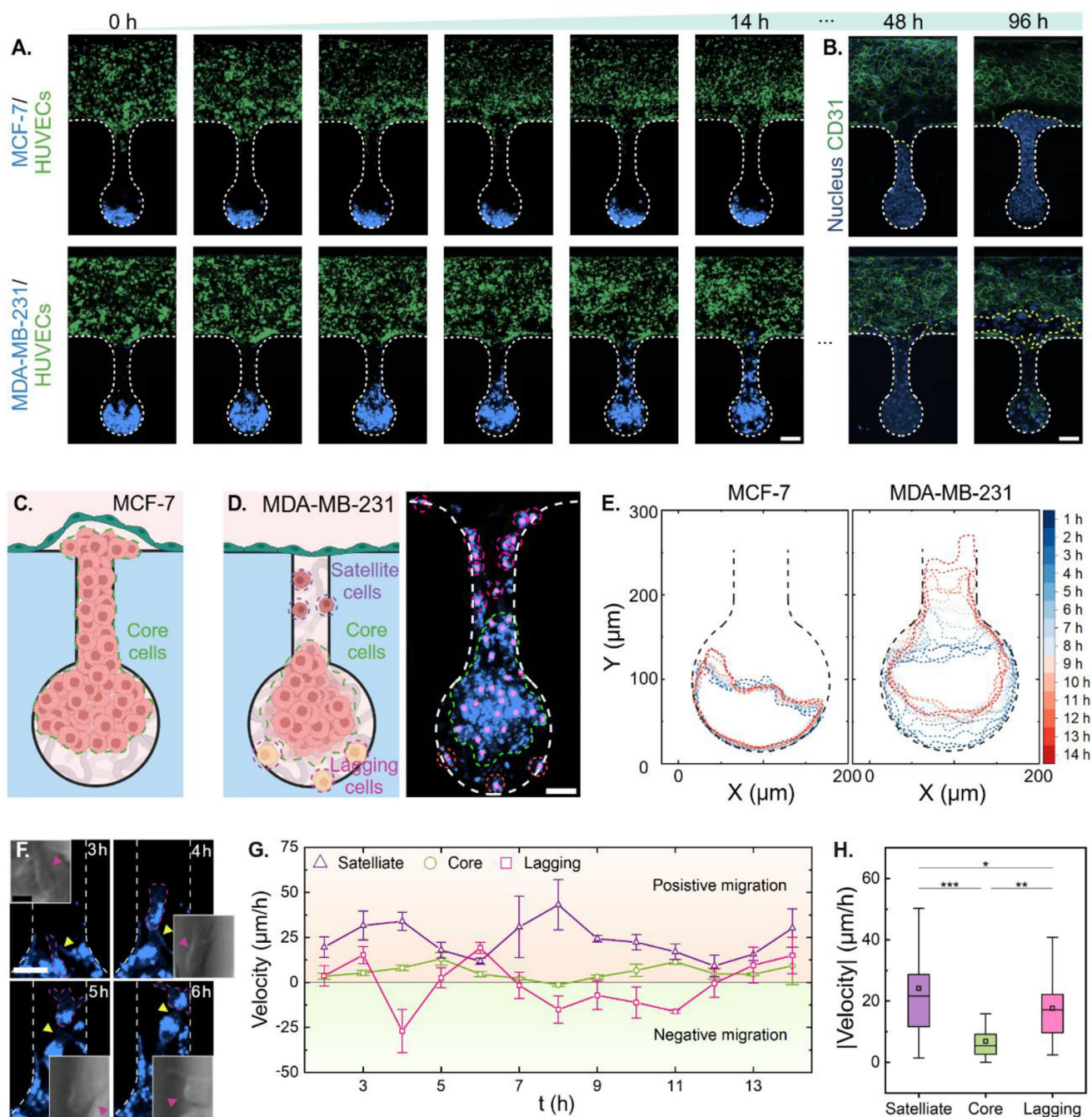


Figure 3. Distinct migratory behaviors of MCF-7 and MDA-MB-231 during intravasation. A, B) Time-lapse imaging demonstrates distinct migration modes of MCF7 (collective invasion) versus MDA-MB-231 (interactive invasion). HUVECs were labeled with PKH67, while MCF7 and MDA-MB-231 were labeled with PKH26 in panel (A). Hoechst 33342 and CD31 were used in panel (B) to label the nucleus and endothelium. Scale bar: 70 μm . C) MCF7 cells display uniform collective migration. D) MDA-MB-231 cells exhibit three distinct populations: satellite cells (leading edge penetration), core cells (progressive margination), and lagging cells (stationary). E) Contour profiles of cancer cells highlighting the distinct migratory behaviors of MDA-MB-231 and MCF7 during intravasation. F) Representative immunofluorescent images showing morphological transformations of MDA-MB-231 cells over 3–6 h. Scale bars: 40 and 15 μm (zoomed-in view). G) Velocity profiles for three different cell populations of MDA-MB-231 from 0 to 14 h. H) Mean velocity of MDA-MB-231 from 0 to 14 h. Data are presented as mean \pm SEM in panel (G). Box plots in (H) indicate the median (middle line), mean (square), the first and third quartiles (box), and the 10th and 90th percentile (error bars) of the velocity. Statistical significance was assessed using One-Way ANOVA (* $p < 0.05$; ** $p < 0.01$; *** $p < 0.001$; $n \geq 3$). Illustration figures are created at <https://BioRender.com>.

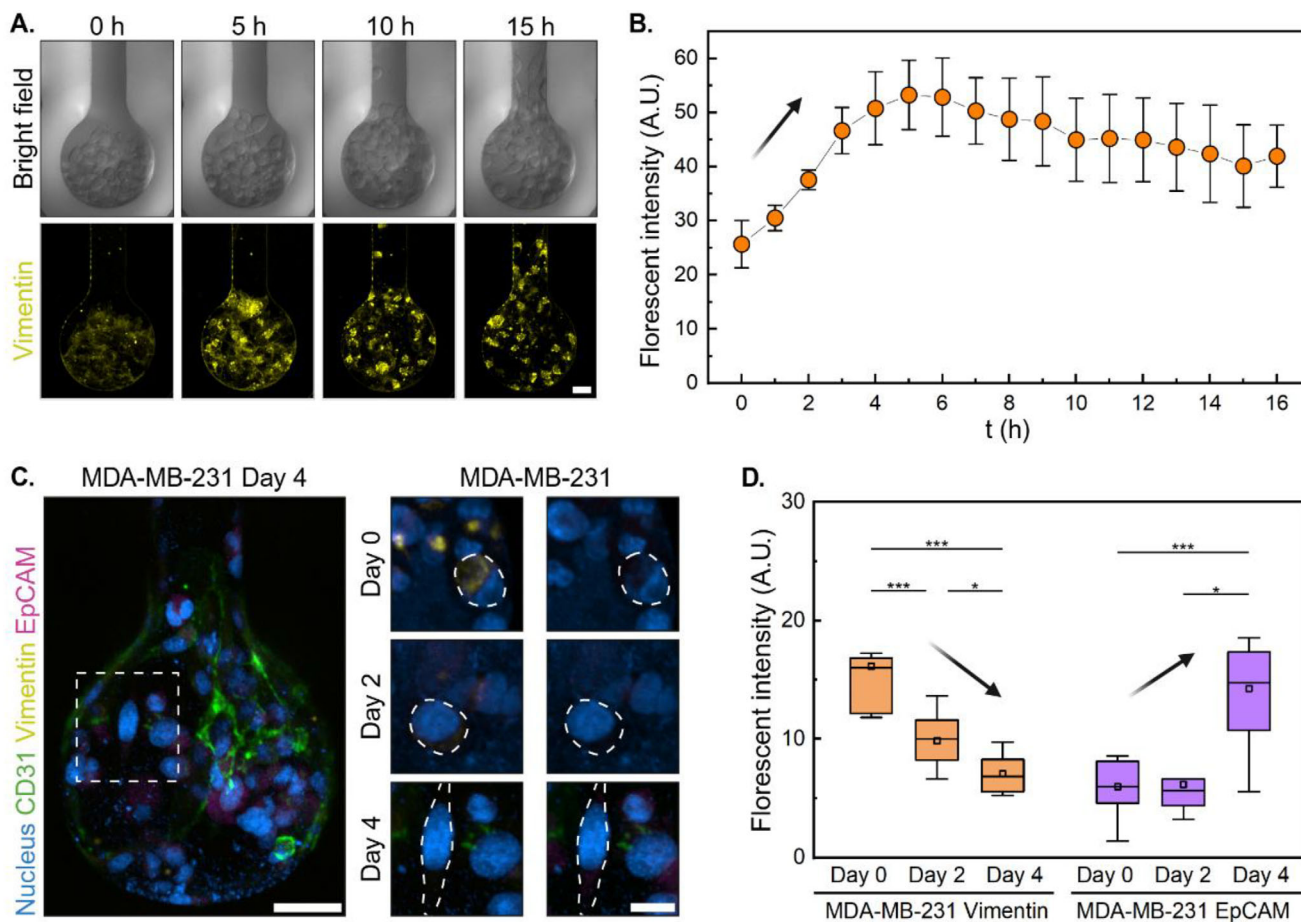


Figure 4. Biphasic EMT-MET dynamics of MDA-MB-231 during intravasation. A) Live cell imaging demonstrates distinct Vimentin variation in MDA-MB-231 cells during the early intravasation phase (0–16 h). Scale bars: 30 μ m. B) Quantitative analysis of Vimentin intensity through cancer-endothelial co-culture from 0 to 16 h, showing initial upregulation followed by decrease. C) Left: Epithelial-mesenchymal transition markers (Vimentin, 1:3000, yellow; EpCAM, 1:400, purple) of MDA-MB-231 co-cultured with HUVECs on day 4. Right: Time-resolved evolution of Vimentin (Yellow, left) and EpCAM (Purple, right) in MDA-MB-231 cells over 4 days. Scale bars: 100 μ m (left) and 20 μ m (right). Time-resolved evolution of epithelial-mesenchymal transition markers (Vimentin, 1:3000, yellow; EpCAM, 1:400, purple) in MDA-MB-231 cells over longer timeframes (0–4 days). Scale bars: 100 μ m (left) and 20 μ m (right). D) Quantitative analysis of EMT marker expression showing an inverse relationship between Vimentin and EpCAM expression over time, indicating MET after initial EMT. Data are presented as arbitrary units (A.U.). Box plots in (D) indicate the median (middle line), mean (square), the first and third quartiles (box), and the 10th and 90th percentile (error bars) of the intensity. Data are presented as mean \pm SEM. Statistical significance was assessed using One-Way ANOVA (* p < 0.05; ** p < 0.01; *** p < 0.001; n \geq 5). Vimentin intensity was quantified using ImageJ from at least 30 cells per timepoint.

2.4. Biphasic EMT-MET Dynamics in Cancer Cells and Endothelial Regulation

Epithelial–mesenchymal dynamics is a biological process where epithelial cells acquire mesenchymal characteristics, enhancing their migratory and invasive capabilities, which is pivotal in cancer progression, particularly during intravasation—the entry of cancer cells into the bloodstream—a critical step in metastasis.^[1,3,35] In our study, we investigated the dynamic expression patterns of Vimentin and EpCAM during intravasation through different time scales.

Our analysis revealed a biphasic pattern of mesenchymal marker expression in MDA-MB-231 cells during intravasation. Time-resolved imaging over the initial 16 h showed that Vimentin expression first increased during the early phase of invasion (Figure 4A,B). Initially, the Vimentin signal was at a relatively low expression level with a quantitative value of 26 (A.U.). From 0 to

5 h, the Vimentin intensity reached its peak value at 53 (A.U.), representing an early EMT phase that promotes initial invasive capabilities. During this phase, MDA-MB-231 cells exhibited enhanced mesenchymal traits, enabling them to navigate through the stromal environment toward the vasculature.

Interestingly, after this initial peak, Vimentin expression began to slightly decrease from 5 to 16 h, stabilizing \approx 40 (A.U.) (Figure 4B). Following that, a further declining trend continued over a longer time scale (within 4 days), with our analysis over 96 h revealing a progressive 2.3 fold decrease in Vimentin expression by day 4 (Figure 4C,D). Concurrently, EpCAM, an epithelial marker, exhibits a 1.5 fold increase within the same time-frame (Figure 4C,D). This inverse relationship suggests a partial mesenchymal-epithelial transition (MET), potentially reducing the metastatic propensity of MDA-MB-231 cells after contacting endothelial cells and promoting cell–cell adhesion and proliferation, which are essential for establishing new tumor colonies. On

the contrary, MDA-MB-231 cells alone did not show such MET transition. There was an enhanced Vimentin expression over 96 h (4.6 fold and 3.8 fold difference, $p < 0.001$ and $p < 0.01$, for static and dynamic culture, respectively) of MDA-MB-231 cells alone compared to HUVECs co-culture group (Figure 5A,C,D; Figures S7 and S8, Supporting Information). This suggests that MDA-MB-231 cells present no tendency toward MET in the absence of endothelial cells. In short, the results indicate that the presence of HUVECs plays a significant role in the modulation of the epithelial-mesenchymal transition process, specifically in MDA-MB-231 cells.

In contrast, MCF-7 cells maintained low Vimentin expression from day 0 to day 4, while EpCAM expression remained consistently high during the same period (Figure 6A). This indicates that MCF-7 cells retain their epithelial characteristics, suggesting a lower invasive potential compared to MDA-MB-231 cells.

Moreover, in the absence of endothelial cells, MDA-MB-231 cells exhibited an advanced invasion pattern. Their distribution from the niche bottom to the main channel can be further categorized into five sub-populations based on morphology and Vimentin expression (Figure 5A,B). Notably, cancer cell migration without endothelial interactions displays a distinct pattern in stage 3, differing from the co-culture system. It is hypothesized that during the transition from stage 2 to stage 3, part of the original satellite cells transforms into a high Vimentin-expressing sub-population, termed primary satellites. These cells exhibit extensive filamentous extensions, forming connections with neighboring cells, indicative of enhanced migratory capacity and intercellular communication. The secondary core likely forms through the migration and amalgamation of the original satellite and core cells. Constrained by geometry, migration is impeded at the top neck region, promoting collective behavior and secondary core formation. The primary core formation may result from neck contraction, permitting only a portion of the cell cluster to migrate. Secondary satellite cells may function as information transmitters, facilitating communication between cores. Quantitative analysis reveals that primary satellite cells express vimentin at levels 2.5-fold higher than primary core cells (Figure 5B and $p < 0.001$), indicating a spatial organization of EMT progression during intravasation.

Such dynamic modulation of the epithelial-mesenchymal markers underscores the plasticity of cancer cells in response to microenvironmental cues.^[40] Our findings highlight the importance of EMT and MET in cancer cell intravasation and subsequent metastatic colonization. Understanding these processes is crucial for developing targeted therapies aimed at inhibiting metastasis by epithelial-mesenchymal transition dynamics.

2.5. Cancer Type-Specific Proliferation and Bilateral Endothelial Interactions

We observed distinct communication patterns between cancer and endothelial cells (Figure 6A,B), with particular emphasis on cancer cell proliferation and density dynamics (Figure 6C,D). MCF-7 cells exhibit a substantial increase in cell number, rising from ≈ 138 cells on day 0 to ≈ 300 cells by day 2 (Figure 6A,C). Correspondingly, cell density escalates from 671 to 875 cells μm^{-2} , indicating robust proliferative activity and spatial expansion

(Figure 6D). In contrast, MDA-MB-231 cells show a modest increase in cell number, from 109 on day 0 to 142 on day 2 (Figure 6B,C). Notably, their cell density decreases from 496 to 238 cells μm^{-2} , suggesting a propensity for dispersal rather than localized proliferation (Figure 6D).

These observations align with the inherent characteristics of the two cell lines. MCF-7 cells, known for their epithelial-like properties, tend to form cohesive clusters, leading to increased cell density as they proliferate. Conversely, MDA-MB-231 cells, which exhibit mesenchymal traits, are more migratory and invasive, often spreading out and reducing local cell density despite an increase in absolute cell numbers.

Furthermore, distinct interaction patterns between cancer cells and endothelial cells at the invasion interface were identified. Notably, MDA-MB-231 cells demonstrated enhanced endothelial attraction compared to MCF-7 cells on day 4, exhibiting a threefold increase in interaction frequency ($p < 0.001$, Figure 6B, E; Figure S9, Supporting Information). This increased interaction was possibly due to the compromised endothelium and Matrigel matrix, which suggests a more aggressive interaction between MDA-MB-231 cells and the endothelial cells, which may facilitate tumor progression and metastasis. This bilateral migration pattern between MDA-MB-231 and endothelial cells closely resembles cancer cell-induced angiogenesis observed *in vivo*^[41,42] and clinically, such as in patients with GBM^[43] and pancreatic cancers,^[44] where aggressive cancer cells attract endothelial cells to form new vessels toward the tumor mass. This behavior may reflect the well-documented secretion of pro-angiogenic factors by MDA-MB-231 cells,^[42,45] which can stimulate endothelial cell migration.

2.6. Differential Endothelial Remodeling and Functional Responses to Cancer Cells

We investigated endothelial reorganization dynamics using two breast cancer cell lines under dynamic medium supply over a 48 h period (Experimental setup is presented in Figure S10, Supporting Information). Spatial mapping revealed distinct patterns of endothelial displacement, particularly evident when comparing proximal and distal regions relative to the cancer-endothelial boundary (Figure 7A; Figure S11, Supporting Information). The MCF-7/HUVECs co-culture showed a uniform displacement pattern, marked by a clear yellow dotted boundary line between cancer and endothelial cells.

Detailed analysis of endothelial adherens junctions (VE-cadherin) and platelet endothelial cell adhesion molecule (CD31) in the main channel revealed cancer type-specific reorganization patterns for proximal and distal regions. The cell bodies of the proximal HUVECs to the MCF-7 cells were bigger and more elongated than the distal ones, which was not observed in HUVECs cocultured with MDA-MB-231 cells (Figure 7B). Cell segmentation analysis (color-coded from 500–3500 μm^2 , indigo to magenta) demonstrated distinct morphological adaptations of endothelial cells in response to different cancer types (Figure 7C). The cell area distributions of HUVECs were analyzed in the presence of MCF-7 and MDA-MB-231 cells. MCF-7 cells induced a significant increase in endothelial cell area at the proximal region (mean area: 1279.58 μm^2) and a decrease at the distal region

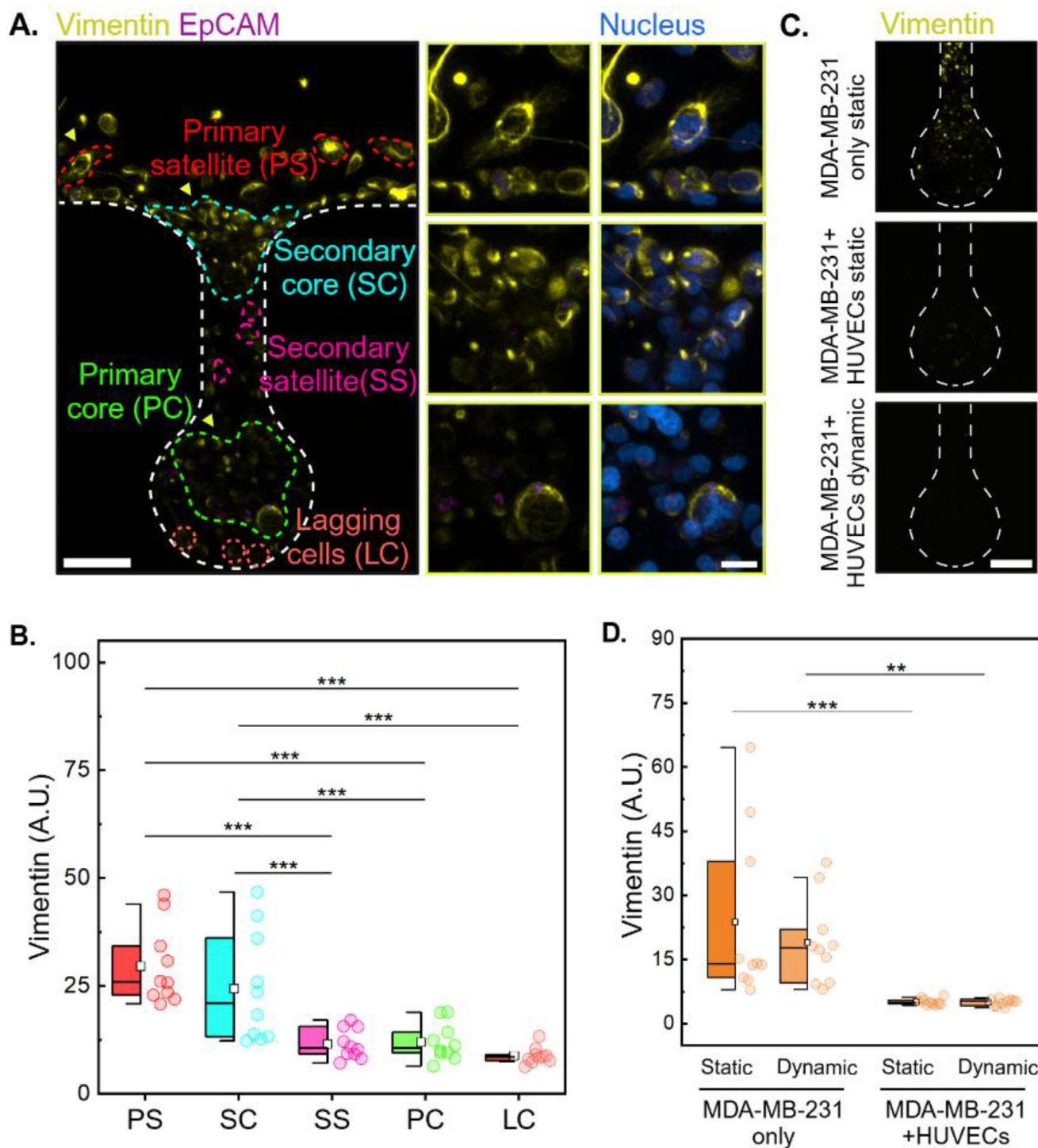


Figure 5. Sub-population-dependent cancer cell mesenchymal marker expression and endothelial inhibitory effect. A) Mapping of MDA-MB-231 mesenchymal marker (vimentin) expression across five distinct cell populations: Lagging cells (LC), primary core (PC), secondary satellite (SS), secondary core (SC), and primary satellite (PS), under dynamic culture conditions without HUVECs for two days. The yellow boxes indicate zoomed-in regions, as pointed to by the yellow arrows. Scale bars: 70 μm (left) and 20 μm (right). B) Quantitative analysis of vimentin expression across different populations of MDA-MB-231. C) Vimentin expression under three other conditions: MDA-MB-231 only static culture, MDA-MB-231+HUVECs static co-culture, and MDA-MB-231+HUVECs dynamic co-culture. Scale bar: 70 μm . D) Quantitative analysis of Vimentin expression across different conditions. Box plots in (B, D) indicate the median (middle line), mean (square), the first and third quartiles (box), and the 10th and 90th percentile (error bars) of the intensity. Statistical significance was determined by One-Way ANOVA or Two-Way ANOVA (** $p < 0.01$; *** $p < 0.001$; $n \geq 5$).

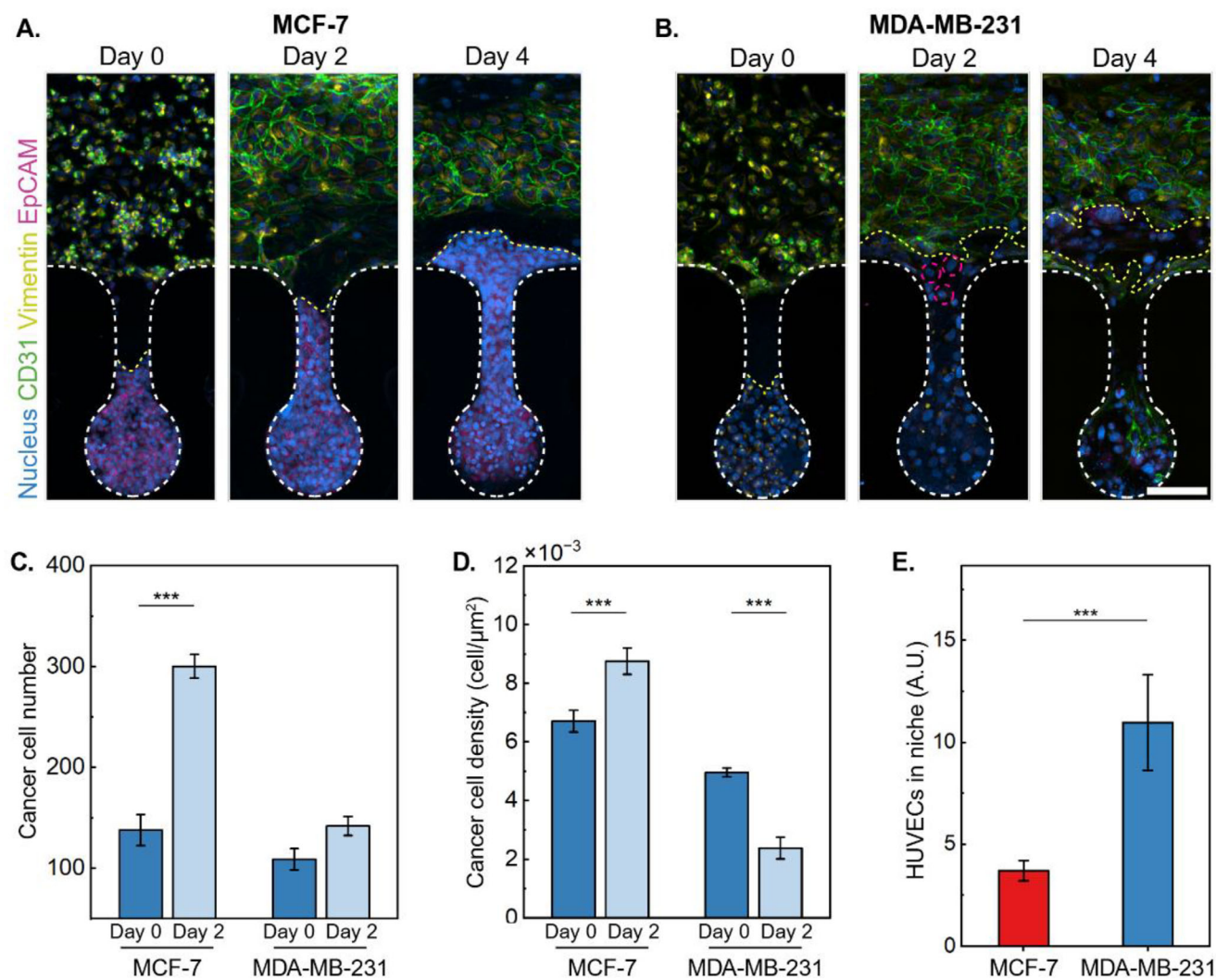


Figure 6. Cancer type-specific proliferation and bilateral cancer-endothelial interactions. Time-resolved imaging reveals two distinct communication patterns between A) MCF-7 and B) MDA-MB-231 co-cultured with endothelial cells over 4 days. CD31 (1:400, green) and Hoechst 33342 (1:1000, blue) were used to label endothelium and nuclei. Pink dotted line indicates the satellite cells. Yellow dotted line indicates the MDA-MB-231 cells that migrated into the main channel. Scale bar: 100 μm. Quantitative analysis of C) cancer cell number and D) cancer cell density (cells μm⁻²), showing different proliferation and spatial organization patterns between the two cancer types. E) Quantitative analysis of cancer-endothelial interactions on day 4, measured by CD31 intensity in niche chambers, showing 3 fold higher endothelial attraction by MDA-MB-231 compared to MCF-7 ($p < 0.001$). Data presented as arbitrary units (A.U.). Data in (C–E) are expressed as mean ± SEM from at least 3 niche chambers per condition. Statistical significance was determined by One-Way ANOVA or Two-Way ANOVA (***) $p < 0.001$; $n \geq 3$). Cell density was calculated by dividing cell number by the measured area occupied within each niche.

(mean area: 230.93 μm²) (Figure 7D). In contrast, MDA-MB-231 cells resulted in a more uniform endothelial cell area distribution, with values ≈600 μm², indicating a less pronounced effect on endothelial cell morphology compared to MCF-7 cells (Figure 7D). Quantitative assessment of aspect ratio distributions showed significant differences between the MCF-7/HUVECs co-culture and HUVECs only (Figure S12A, Supporting Information) ($p < 0.01$).

Fluorescent intensity profiles of VE-cadherin and CD31 along the main channel width revealed gradient patterns specific to each cancer type (Figure 7E; Figure S12B, Supporting Information). The MDA-MB-231/HUVECs co-culture showed more pronounced junction reorganization in the proximal region compared to the MCF-7/HUVECs co-culture (3 fold difference).

To further validate the functionality of the endothelium and examine the effect of cancer cells on endothelial activation, we investigated ICAM-1 expression following PMA treatment under different culture conditions. The experiment consisted of four groups: HUVECs only with or without PMA treatment as well as the co-culture of HUVECs and MDA-MB-231 cells with or without PMA treatment (Figure 8A). The results demonstrated a significant upregulation of ICAM-1 in HUVECs only upon PMA stimulation (3 fold higher, $p < 0.01$) (Figure 8A,B), confirming the responsiveness of our endothelial model to inflammatory stimuli. Remarkably, ICAM-1 expression was even higher in the presence of MDA-MB-231 cells, regardless of PMA treatment (5.5 fold higher, $p < 0.001$) (Figure 8A,B).

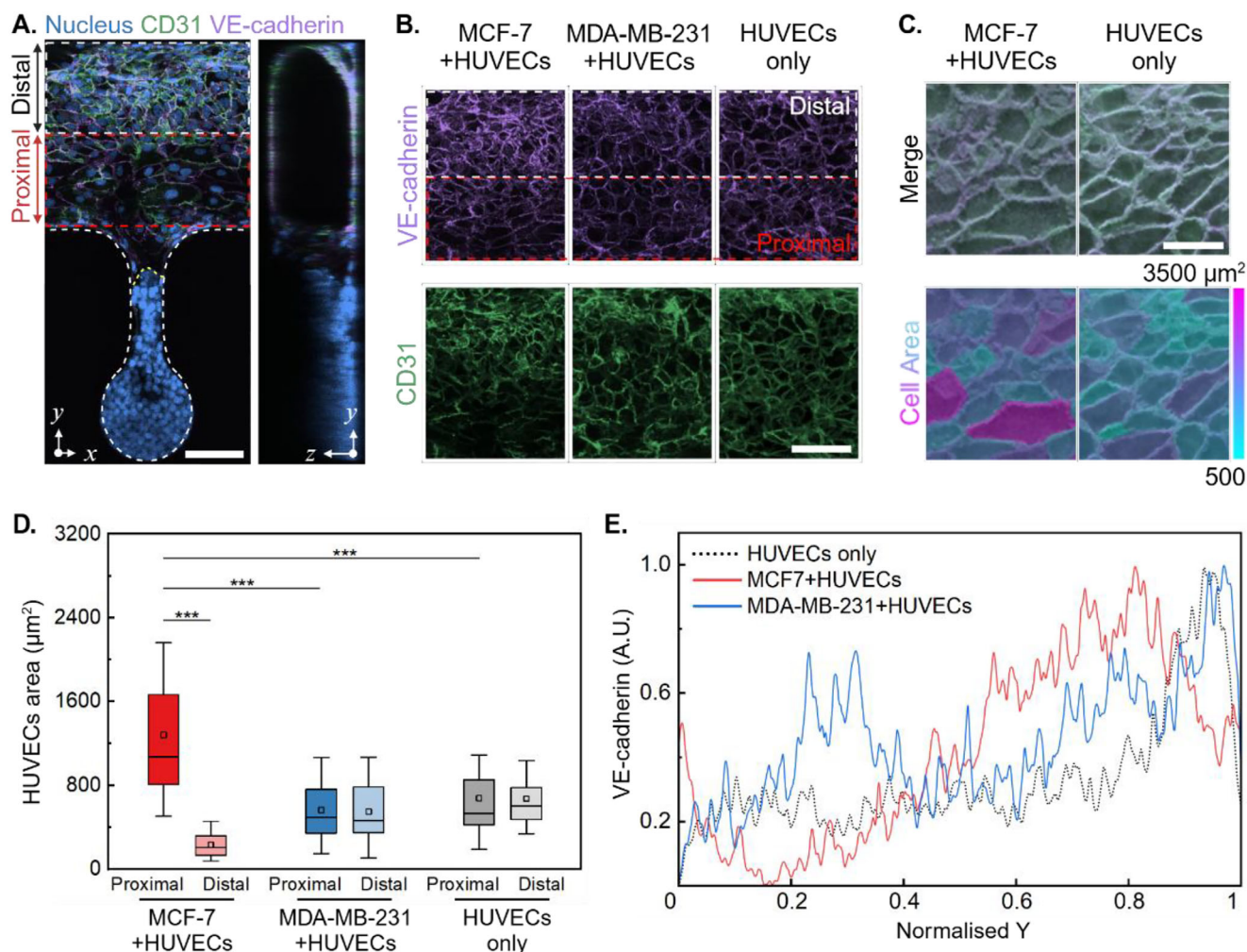


Figure 7. Differential endothelial remodeling responses to cancer cell types. A) Spatial mapping of HUVECs and cancer cells under dynamic culture conditions ($1.875 \mu\text{L min}^{-1}$, 48 h). The main channel is divided into distal and proximal regions. The yellow dotted line indicates the cancer cell-endothelial cell boundary. Scale bar: $100 \mu\text{m}$. B) Confocal images of the endothelium in the main channel showing endothelial adherent junctions (VE-cadherin, 1:400, purple) and platelet endothelial cell adhesion molecule (CD31, 1:400, green). Scale bar: $100 \mu\text{m}$. C) Endothelial cell segmentation performed using the automated algorithm in ImageJ. Color bar: cell area from 500 to $3500 \mu\text{m}^2$ (indigo to magenta). D) Comparative analysis of HUVECs cell area (CA) distributions, showing significant morphological differences between proximal and distal regions in MCF-7 co-culture. E) VE-cadherin intensity profile measured along main channel width, showing gradient patterns specific to each cancer type. Box plots in (E) indicate the median (middle line), mean (square), the first and third quartiles (box), and the 10th and 90th percentile (error bars) of the HUVECs CA. Statistical significance was determined by Two-Way ANOVA ($***p < 0.001$; $n \geq 30$).

This pronounced effect in the co-culture conditions suggests that cancer cells strongly influence endothelial activation. MDA-MB-231 cells may induce ICAM-1 expression, possibly due to the secretion of pro-inflammatory cytokines such as $\text{TNF-}\alpha$ and $\text{IL-1}\beta$,^[46,47] which are known to enhance endothelial adhesion molecule expression. Additionally, direct cell–cell interactions between cancer cells and endothelial cells could activate signaling pathways that upregulate ICAM-1. Given that co-culture lasted for 24 h, it is predicted that the sustained influence of cancer cell-derived signals outweighed the transient effects of PMA stimulation (1.5 h). This finding highlights the critical role of tumor-endothelial interactions in modulating endothelial function and adhesion molecule expression, which may have implications for cancer cell intravasation and metastasis.

3. Discussion, Conclusion, and Future Perspectives

The INVADE platform represents a significant advancement in studying cancer cell intravasation, providing unprecedented insights into the dynamic interactions between cancer cells and the endothelial barrier. Through this work, we have demonstrated four key findings: 1) the existence of distinct intravasation modes between different cancer cell types, 2) the critical role of endothelium-regulated EMT-MET dynamics during cancer intravasation, 3) the bilateral interaction between cancer cells and endothelial cells, and 4) the differential inflammatory response of endothelium to cancer cells.

Our comprehensive platform validation confirmed the establishment of a functional endothelial barrier with intact junction

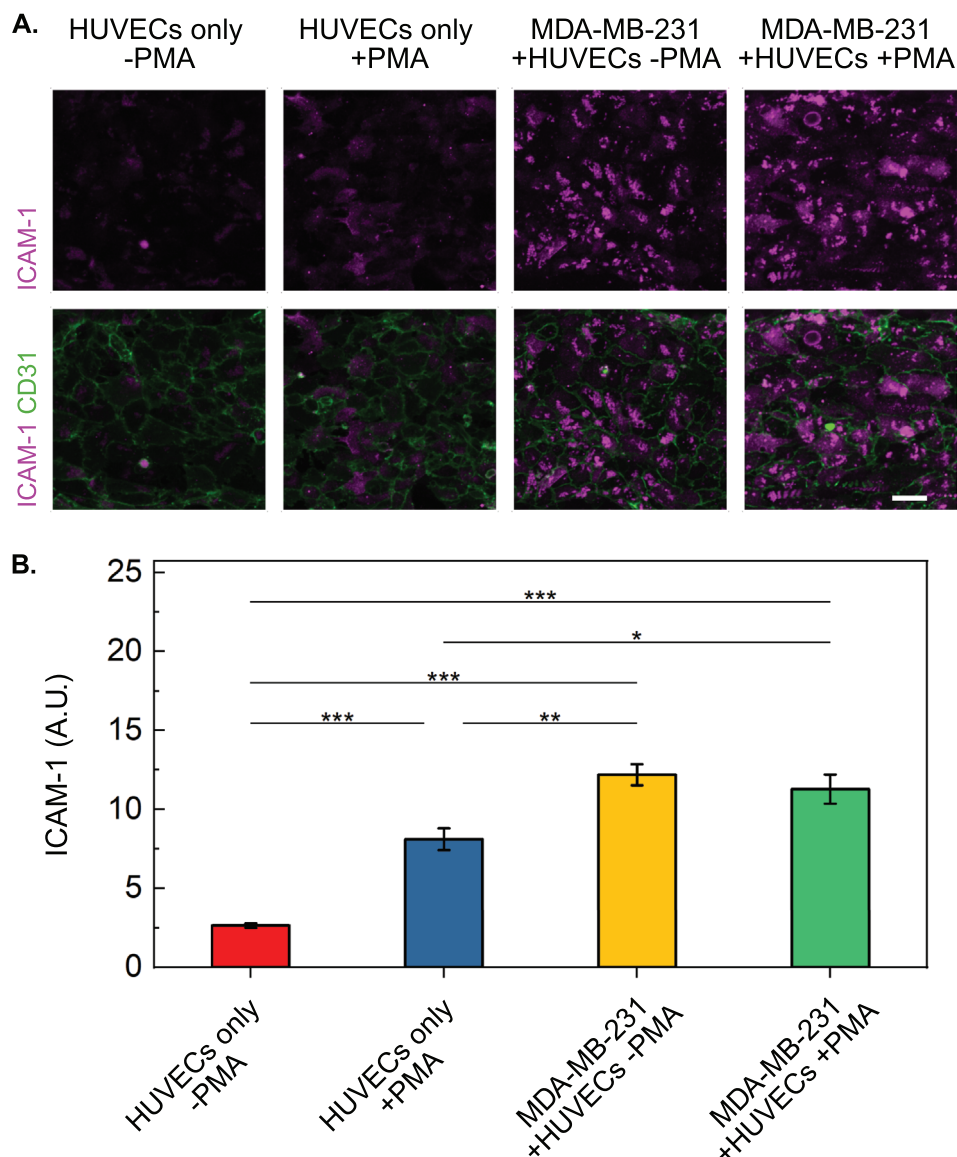


Figure 8. Endothelial ICAM-1 expression in response to co-culture with cancer cells and PMA stimulation. A) Fluorescent images of endothelium showing intercellular adhesion molecule 1 (ICAM-1, 1:200, magenta) and platelet endothelial cell adhesion molecule (CD31, 1:300, green) in the main channel under four conditions: HUVECs only (\pm PMA) and HUVECs+MDA-MB-231 co-culture (\pm PMA). PMA was applied at 50 ng mL^{-1} for 1.5 h before fixation. Scale bar: $50 \mu\text{m}$. B) Quantitative analysis of ICAM-1 expression across different conditions, showing significant upregulation in HUVECs upon PMA stimulation (3-fold higher, $p < 0.01$) and even higher expression in the presence of MDA-MB-231 cells regardless of PMA treatment (5.5 fold higher, $p < 0.001$). Data are expressed as mean \pm SEM from at least 3 regions of interest per condition. Statistical significance was determined by One-Way ANOVA ($^*p < 0.05$; $^{**}p < 0.01$; $^{***}p < 0.001$; $n \geq 3$).

complexes before cancer-endothelial interactions begin, as evidenced by FITC-Dextran diffusion studies and z-stack confocal imaging. The physiological responsiveness of endothelium within INVADE was further validated by ICAM-1 upregulation following PMA stimulation, addressing concerns about endothelial barrier functionality at the critical neck-channel interface.

Our results reveal fundamentally different intravasation strategies between MCF-7 and MDA-MB-231 breast cancer cells. MCF-7 cells exhibited collective invasion behavior, moving as a cohesive unit that physically expels the endothelial barrier. In contrast, MDA-MB-231 cells demonstrated a more sophisticated in-

teractive invasion mode characterized by three distinct subpopulations: satellite cells, which act as pioneers in contacting the endothelium with the highest motility ($24.1 \mu\text{m h}^{-1}$), core cells that maintain coordinated forward movement ($6.7 \mu\text{m h}^{-1}$), and lagging cells that remain in the deep bottom of niche.^[14,48]

A particularly novel finding from our study is the dynamic regulation of EMT markers during intravasation. MDA-MB-231 cells co-cultured with HUVECs showed a progressive 2.3 fold decrease in Vimentin expression accompanied by a 1.5 fold increase in EpCAM over 96 h, suggesting a partial MET. In stark contrast, MDA-MB-231 cells cultured without endothelial cells

showed enhanced Vimentin expression with no tendency toward MET. This endothelial-induced MET may represent an adaptive mechanism that facilitates the successful completion of the intravasation process.^[49,50]

When MDA-MB-231 cells were cultured independently of HUVECs, primary satellite cells exhibited the highest Vimentin expression, demonstrating a 2.5 fold increase compared to primary core cells. This spatial distribution highlights a hierarchical organization in EMT progression during cancer migration.^[51] To that end, while geometric constraints can influence cell migration patterns as demonstrated by Friedl et al.,^[52] our comparative analyses between cancer cells cultured with or without endothelial cells under identical geometrical conditions strongly suggest that the observed phenotypic changes in our current INVADE system are primarily driven by endothelial interactions rather than physical confinement.

The INVADE platform overcomes several limitations of existing approaches through its unique features: 1) high-throughput capability ($n = 23$ parallel units) enabling robust statistical analysis while maintaining experimental consistency; 2) precise control over micro-environment and geometries allowing investigation of programmable cancer-endothelial interactions; 3) clear visualization of cellular dynamics through optimized optical properties and selective surface modification; 4) maintenance of distinct microenvironments through careful compartmentalization (>99% endothelial confluence under flow).

Last but not least, future studies should explore the molecular mechanisms underlying cancer-endothelial crosstalk and investigate how various geometrical constraints might influence cancer cell behaviors. To that end, future iterations of the INVADE platform could systematically vary confinement geometries to disentangle mechanical effects from biochemical signaling. These insights would further advance our understanding of cancer metastasis and suggest new therapeutic strategies targeting the cancer-endothelial interface.

4. Experimental Section

Microfabrication: The INVADE microfluidic device was fabricated using standard soft lithography techniques.^[53,54] Briefly, a 200 μm constant height dry photoresist film (D) micro laminate SUEX) was laminated on the silicon wafer at 85 $^{\circ}\text{C}$ to create the channel using a direct lithography writer (Heidelberg MLA-100, 4500 m^2cm^{-2}). When the lithography was finished, the wafer was taken for 5 min post-baking at 90 $^{\circ}\text{C}$, followed by PGMEA rinsing until the excess photoresist was completely removed. Polydimethylsiloxane (PDMS, Sylgard 184, Dow Corning) was mixed at a 10:1 ratio (w/w) of elastomer to curing agent, degassed, and poured over the master mold. After curing at 100 $^{\circ}\text{C}$ for 1.5 h, the PDMS layer was carefully peeled off, and access holes were punched using a 1.5 mm biopsy punch. The PDMS layer was bonded to the PDMS membrane using a plasma cleaner (Harrick Plasma).

Surface Modification and Device Preparation: The INVADE platform underwent selective surface modification to create distinct microenvironments. Niche chambers were treated with Pluronic F-127 (0.5% w v^{-1} in PBS) for 30 min at room temperature to prevent cell adhesion. The main channel was subsequently coated with fibronectin (100 $\mu\text{g mL}^{-1}$) for 1 h at 37 $^{\circ}\text{C}$ to promote endothelial cell attachment.

Cell Culture and Microfluidic Seeding: Human breast adenocarcinoma cells (MCF-7 and MDA-MB-231) were obtained from ATCC and maintained in DMEM supplemented with 10% FBS and 1% penicillin/streptomycin. Human Umbilical Vein Endothelial Cells (HUVECs, passage 3–6) were cultured in an endothelial growth medium (EGM-2,

Lonza). All cells were maintained at 37 $^{\circ}\text{C}$ with 5% CO_2 and passaged at 80% confluence. Cells were harvested from devices using TrypLE treatment for 5 min before seeding.

Cancer cell seeding was performed using a mixture of cell suspension (1×10^6 cells mL^{-1}) and Matrigel (2:1 volume ratio). Following vacuum treatment (> 30 min), the mixture was introduced into niche chambers and centrifuged (2000 rpm, 30 s). After 15 min incubation on ice and 30 min incubation at 37 $^{\circ}\text{C}$, a second Matrigel (mixed with a medium at 1:1 volume ratio) layer was added to seal the neck region. Similar to our previous works,^[5,55] HUVECs (1×10^7 cells mL^{-1}) were seeded into the fibronectin-coated main channel and allowed to attach for 30 min under static conditions. The microchip was turned over to facilitate both sides of the attachment. Dynamic culture was maintained using a syringe pump delivering culture medium at 1.875 $\mu\text{L min}^{-1}$ (corresponding to 0.5 dyne cm^{-2} shear stress).

Live imaging staining: For fluorescent live imaging, cancer cells were stained with PKH26 Red Fluorescent Cell Linker Kit and HUVECs with PKH67 Green Fluorescent Cell Linker Kit (Sigma-Aldrich). Both cancer cells and HUVECs were stained with BioTracker TiY Vimentin Live Cell Dye (Sigma-Aldrich) following manufacturer's protocols. Matrigel (Growth Factor Reduced, Corning) was mixed with cancer cell suspension at 1:2 volume ratio before seeding. Fibronectin solution (100 $\mu\text{g mL}^{-1}$ in PBS) was prepared fresh for each experiment. Fluorescein isothiocyanatedextran (FITC-Dex, 3- to 5-kDa, Sigma-Aldrich) was prepared fresh at concentration of 1 mg mL^{-1} for diffusion experiment. To examine the endothelium functionality, phorbol-12-myristate-13-acetate (PMA) with concentration of 50 ng mL^{-1} in serum-free medium EGM-2 was added into the channel and incubated at 37 $^{\circ}\text{C}$ for 1.5 h before imaging.

Immunofluorescence Staining: Cells were fixed with 4% paraformaldehyde for 1 h and then washed with PBS for 1 h. Cells were then permeabilized with 1% Triton X-100 for 2 h and blocked with 3% BSA overnight in 4 $^{\circ}\text{C}$ fridge. Primary antibodies with fluorescence against CD31 (1:400), VE-cadherin (1:400), Vimentin (1:3000), EpCAM (1:400), and Hoechst 33342 (1:1000) were incubated on a shaker for 3 days at room temperature. Afterward, PBS was added to wash the channel on a shaker for 2 days. To investigate ICAM-1 expression in the main channel, cells were fixed with 4% paraformaldehyde for 10 min and then incubated with CD31 (1:300) and ICAM-1 (1:200) for 1 h at 37 $^{\circ}\text{C}$.

Image Acquisition and Analysis: Time-lapse imaging was performed using an environmentally controlled confocal microscope (Olympus FV3000RS) equipped with a 20 \times objective (NA 0.8). For z-stack imaging to validate endothelial barrier integrity, confocal images were captured at different heights (50, 100, 150, and 200 μm) along the z-axis using a 20 \times objective (NA 0.8). For endpoint analyses, high-resolution confocal images were captured with a 2 μm z-step size. FITC-Dextran diffusion was imaged using the epifluorescence mode with a 20 \times objective at 30 and 60 s after injection. Image analysis was performed using ImageJ/FIJI software. Cell tracking was conducted using the Imaris (Bitplane AG, Oxford Instruments). Cell morphology parameters were analyzed using ImageJ/FIJI software. Fluorescence intensity profiles were generated using the Plot Profile function in ImageJ.

Statistical Analysis: All experiments were performed with at least three biological replicates. Statistical analysis was performed using Origin software (OriginPro 2024). One-Way ANOVA and Two-Way ANOVA with Fisher's Least Significant Difference (LSD) test was used for multiple comparisons. Data are presented as mean \pm SEM of $n \geq 3$, with $p < 0.05$ considered statistically significant.

Supporting Information

Supporting Information is available from the Wiley Online Library or from the author.

Acknowledgements

The authors would like to thank ZuFu Lu, Hala Zreiqat, and Gungun Lin for lab facility support; thank Wenlong Cheng, Yunduo (Charles) Zhao,

and Arian Nassar for the technical support and paper structuring; thank Nelson Briones, Ethel Ilagan, Jacky He, for assistance in soft lithography. This work was conducted (in part) using the Research Prototype Foundry core research facilities at the NSW node of the Australian National Fabrication Facility (ANFF-NSW), a company established under the National Collaborative Research Infrastructure Strategy to provide nano- and micro-fabrication facilities for Australia's researchers. Thank Tina Lin, and Young No for tissue culture support; thank Tong Wu, Xinlin Zheng, and Lixin Zhang from Evident Australia for microscopy instrumentation and imaging support. This work was supported by the NSW Cardiovascular Capacity Building Program (Early-Mid Career Researcher Grant – L.A.J.; H22/98586–K.L.); the ARC Discovery Project Grants (DP240102315–L.A.J.; DP240101768–L.A.J.); MRFF Cardiovascular Health Mission Grant Round (MRF2023977–L.A.J.); Tour de Cure Annual Grant, Pioneering Research Grants (RSP-391-FY2023–L.A.J. and Y.W.); National Heart Foundation Vanguard Grant (106979–L.A.J.); the International Partnership Program of Chinese Academy of Sciences (Grant 030GJHZ2023098FN and 030GJHZ2024103MI H.L.). Lining Arnold Ju is a Snow Medical Research Foundation Fellow (2022SF176) and a National Heart Foundation Future Leader Fellow Level 2 (105863); Khoon Lim is an Australian Research Council Future Fellow (FT230100249). [Correction added on April 17, 2025, after first online publication: Acknowledgement section has been updated.]

Open access publishing facilitated by The University of Sydney, as part of the Wiley - The University of Sydney agreement via the Council of Australian University Librarians.

Conflict of Interest

The authors declare no conflict of interest.

Author Contributions

F.J., H.L., and L.A.J. proposed research ideas and designed. F.J. performed the experiments, and established the INVADE platform, analyzed the data and prepared the manuscript. Y.Z. performed immunostaining and analysis. G.F., Y.W., Y.S., Y.W., K.S., Y.S.Z., A.C., and H.L. provided intellectual contribution to the tissue engineering in INVADE system along with critical suggestions to the technology development. J.J. and A.D. provided tissue culture support and quality controls. L.A.J. is the senior author who supervised the study and provided instruction, design suggestions for the improvement of the experiments. All authors provided comments and corrections to the manuscript writing.

Data Availability Statement

The data that support the findings of this study are available from the corresponding author upon reasonable request.

Keywords

cancer metastasis, endothelium, epithelial-mesenchymal transition, intravasation, microfluidics, vimentin

Received: January 21, 2025

Revised: March 19, 2025

Published online: April 13, 2025

[1] C. L. Chaffer, R. A. Weinberg, *Science* **2011**, 331, 1559.

[2] K. E. de Visser, J. A. Joyce, *Cancer Cell* **2023**, 41, 374.

- [3] N. Reymond, B. B. Agua d', A. J. Ridley, *Nat. Rev. Cancer* **2013**, 13, 858.
- [4] I. K. Zervantonakis, S. K. Hughes-Alford, J. L. Charest, J. S. Condeelis, F. B. Gertler, R. D. Kamm, *Proc Natl Acad Sci U S A* **2012**, 109, 13515.
- [5] Y. Zhang, F. Jiang, Y. C. Zhao, A. N. Cho, G. Fang, C. D. Cox, H. Zreiqat, Z. F. Lu, H. Lu, L. A. Ju, *Biomed. Mater.* **2023**, 18, 055008.
- [6] H.-W. Cheng, Y.-F. Chen, J.-M. Wong, C.-W. Weng, H.-Y. Chen, S.-L. Yu, H.-W. Chen, A. Yuan, J. J. W. Chen, *J. Exper. Clin. Cancer Res.* **2017**, 36, 27.
- [7] A. Lainé, O. Labiad, H. Hernandez-Vargas, S. This, A. Sanlaville, S. Léon, S. Dalle, D. Sheppard, M. A. Travis, H. Paidassi, J. C. Marie, *Nat. Commun.* **2021**, 12, 6228.
- [8] K. Jiang, S. B. Lim, J. Xiao, D. S. Jokhun, M. Shang, X. Song, P. Zhang, L. Liang, B. C. Low, G. V. Shivashankar, C. T. Lim, *Adv. Sci. (Weinh)* **2023**, 10, 2201663.
- [9] W. J. Polacheck, A. E. German, A. Mammoto, D. E. Ingber, R. D. Kamm, *Proc Natl Acad Sci U S A* **2014**, 111, 2447.
- [10] X. C. Li, J. L. Wang, *Int. J. Biol. Sciences* **2020**, 16, 2014.
- [11] G. Follain, D. Herrmann, S. Harlepp, V. Hyenne, N. Osmani, S. C. Warren, P. Timpson, J. G. Goetz, *Nat. Rev. Cancer* **2020**, 20, 107.
- [12] F. Font-Clos, S. Zapperi, C. A. M. La Porta, *iScience* **2020**, 23, 101073.
- [13] N. Rahmati, N. Maftoon, *Front. Bioeng. Biotechnol.* **2024**, 12.
- [14] D. X. Nguyen, P. D. Bos, J. Massague, *Nat. Rev. Cancer* **2009**, 9, 274.
- [15] M. Park, D. Kim, S. Ko, A. Kim, K. Mo, H. Yoon, *Int. J. Mol. Sci.* **2022**, 23, 6806.
- [16] K. Grubczak, A. Kretowska-Grunwald, D. Groth, I. Poplawska, A. Eljaszewicz, L. Bolkun, A. Starosz, J. M. Holl, M. Mysliwiec, J. Kruszewska, M. Z. Wojtukiewicz, M. Moniuszko, *Cells* **2021**, 10, 2044.
- [17] S. Bersini, J. S. Jeon, M. Moretti, R. D. Kamm, *Drug Discov. Today* **2014**, 19, 735.
- [18] K. E. Sung, D. J. Beebe, *Adv Drug Deliv. Rev.* **2014**, 79–80, 68.
- [19] S. N. Bhatia, D. E. Ingber, *Nat. Biotechnol.* **2014**, 32, 760.
- [20] M. B. Chen, J. A. Whisler, J. Frose, C. Yu, Y. Shin, R. D. Kamm, *Nat. Protoc.* **2017**, 12, 865.
- [21] X. Shen, C. Wang, H. Zhu, Y. Wang, X. Wang, X. Cheng, W. Ge, W. Lu, *J. Ovarian. Res.* **2021**, 14, 38.
- [22] J. Li, Q. Guo, X. Lei, L. Zhang, C. Su, Y. Liu, W. Zhou, H. Chen, H. Wang, F. Wang, Y. Yan, J. Zhang, *J. Cancer* **2020**, 11, 6348.
- [23] R. Augustine, A. A. Zahid, F. Mraiche, K. Alam, A. E. Al Moustafa, A. Hasan, *Pharm. Dev. Technol.* **2021**, 26, 490.
- [24] M. Hakim, L. Kermanshah, H. Abouali, H. M. Hashemi, A. Yari, F. Khorasheh, I. Alemzadeh, M. Vossoughi, *Biophys. Rev.* **2022**, 14, 517.
- [25] P. Mehta, Z. Rahman, P. ten Dijke, P. E. Boukany, *Trends Cancer* **2022**, 8, 683.
- [26] S. Bersini, J. S. Jeon, G. Dubini, C. Arrigoni, S. Chung, J. L. Charest, M. Moretti, R. D. Kamm, *Biomaterials* **2014**, 35, 2454.
- [27] Y. Zhang, S. D. Z. Ramasundara, R. E. Preketes-tardiani, V. Cheng, H. Lu, L. A. Ju, *Frontiers in Cardiovascular Medicine* **2021**, 8, 766513.
- [28] I. Sigdel, N. Gupta, F. Faizee, V. M. Khare, A. K. Tiwari, Y. Tang, *Front. Bioeng. Biotechnol.* **2021**, 9, 633671.
- [29] S. Devarasou, M. Kang, J. H. Shin, *APL Bioeng.* **2024**, 8, 021507.
- [30] V. Azimian Zavareh, L. Rafiee, M. Sheikholeslam, L. Shariati, G. Vaseghi, H. Savoji, S. Haghjooy Javanmard, *ACS Biomater. Sci. Eng.* **2022**, 8, 4648.
- [31] F. Paradiso, S. Serpelloni, L. W. Francis, F. Taraballi, *Int. J. Mol. Sci.* **2021**, 22, 10098.
- [32] C. D. Paul, P. Mistriotis, K. Konstantopoulos, *Nat. Rev. Cancer* **2017**, 17, 131.
- [33] B. Strlic, S. Offermanns, *Cancer Cell* **2017**, 32, 282.
- [34] M. K. Sznurkowska, N. Aceto, *FEBS J.* **2022**, 289, 4336.
- [35] A. Nurmagametova, V. Mustyatsa, A. Saidova, I. Vorobjev, *Sci. Rep.* **2023**, 13, 22164.
- [36] H. T. Morris, L. M. Machesky, *Br. J. Cancer* **2015**, 112, 613.
- [37] C. T. Mierke, *Rep. Prog. Phys.* **2019**, 82, 064602.

- [38] C. Z. Eddy, H. Raposo, A. Manchanda, R. Wong, F. Li, B. Sun, *Sci. Rep.* **2021**, *11*, 20434.
- [39] J. Fares, M. Y. Fares, H. H. Khachfe, H. A. Salhab, Y. Fares, *Signal Transduct Target Ther* **2020**, *5*, 28.
- [40] A. Martowicz, G. Spizzo, G. Gastl, G. Untergasser, *BMC Cancer* **2012**, *12*, 501.
- [41] T. Tonini, F. Rossi, P. P. Claudio, *Oncogene* **2003**, *22*, 6549.
- [42] P. Carmeliet, R. K. Jain, *Nature* **2000**, *407*, 249.
- [43] B. K. Ahir, H. H. Engelhard, S. S. Lakka, *Mol. Neurobiol.* **2020**, *57*, 2461.
- [44] T. Annese, R. Tamma, S. Ruggieri, D. Ribatti, *Cancers (Basel)* **2019**, *11*, 381.
- [45] E. J. Sohn, D. B. Jung, H. Lee, I. Han, J. Lee, H. Lee, S. H. Kim, *Cancer Lett.* **2018**, *412*, 88.
- [46] Y. Kawai, M. Kaidoh, T. Ohhashi, *Am. J. Physiol. Cell Physiol.* **2008**, *295*, C1123.
- [47] L. Wang, D. D. Du, Z. X. Zheng, P. F. Shang, X. X. Yang, C. Sun, X. Y. Wang, Y. J. Tang, X. L. Guo, *Front. Pharmacol.* **2022**, *13*, 979474.
- [48] S. M. Weis, D. A. Cheresh, *Nat. Cell Biol.* **2013**, *15*, 721.
- [49] J. W. Song, L. L. Munn, *Proc. Natl Acad. Sci. USA* **2011**, *108*, 15342.
- [50] D. Wirtz, K. Konstantopoulos, P. C. Searson, *Nat. Rev. Cancer* **2011**, *11*, 512.
- [51] N. Osmani, G. Follain, M. J. G. León, O. Lefebvre, I. Busnelli, A. Larnicol, S. Harlepp, J. G. Goetz, *Cell Rep.* **2019**, *28*, 2491.
- [52] A. Haeger, M. Krause, K. Wolf, P. Friedl, *Biochim. Biophys. Acta.* **2014**, *1840*, 2386.
- [53] L. A. Ju, S. Kossmann, Y. C. Zhao, L. Moldovan, Y. Zhang, S. De Zoysa Ramasundara, F. Zhou, H. Lu, I. Alwis, S. M. Schoenwaelder, Y. Yuan, S. P. Jackson, *The Analyst* **2022**, *147*, 1222.
- [54] G. Fang, H. Lu, R. Al-Nakashli, R. Chapman, Y. Zhang, L. A. Ju, G. Lin, M. H. Stenzel, D. Jin, *Biofabrication* **2021**, *14*, 015006.
- [55] Y. Zhang, S. Aye, V. Cheng, A. Nasser, T. Hong, P. Vatankhah, F. Jiang, Y. C. Zhao, L. Moldovan, A. Sun, A. Dupuy, Y. Wang, Z. Li, T. Ang, F. Passam, K. Yong, L. A. Ju, *Adv. Mater. Interfaces* **2023**, *10*, 2300234.